Research Papers

GREENSUSMATER

Greensusmater
Vol. 3, No. 2, 2026, 10
https://doi.org/10.62755/gsm.2026.10

Check for updates

# Effect of Precursor-Solution pH on the Phase Composition and Microstructure of Precipitated NiO, and By-Product Retention in Hydrothermally Derived NiO–$MnO_2$ Powders

Bayu Prasetya[1,*], Jihan F. Naila[1], Resti Marlina[3], Wahyu S. Sipahutar[1], Eka Nurfani[1,2,*]

[1] *Department of Materials Engineering, Faculty of Industrial Technology, Institut Teknologi Sumatera (ITERA), South Lampung 35365, Indonesia*
[2] *Center for Green and Sustainable Materials, Institut Teknologi Sumatera (ITERA), South Lampung 35365, Indonesia*
[3] *Research Center for Biomass and Bioproducts, National Research and Innovation Agency (BRIN), South Tangerang 15314, Indonesia*

**Corresponding authors**: bayu.prasetya@mt.itera.ac.id; eka.nurfani@mt.itera.ac.id

ARTICLE HISTORY: Received: July 25, 2026 | Revised: October 1, 2026 | Accepted: October 10, 2026

## ABSTRACT

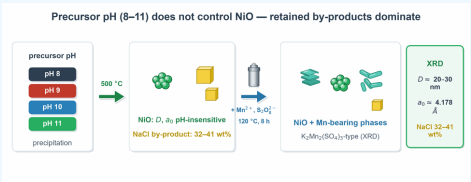


Nickel oxide (NiO)/manganese dioxide ($MnO_2$) composites are widely studied pseudocapacitive electrode materials, but the role of the precursor-solution pH in their synthesis is poorly established. NiO was precipitated at precursor pH 8, 9, 10, and 11, calcined, and subjected to a hydrothermal $MnO_2$-growth step, and the products were characterized by X-ray diffraction (XRD), field-emission scanning electron microscopy (FE-SEM), and energy-dispersive X-ray spectroscopy (EDS). Cubic NiO was the only Ni-bearing oxide, accompanied by a large halite (NaCl) by-product fraction (32–41 wt%). Scherrer, Williamson–Hall, and size–strain-plot analyses gave a NiO crystallite size of 20–30 nm and a microstrain near $1\times10^{-3}$, and Nelson–Riley refinement gave a lattice parameter of 4.178 Å, equal to the bulk value; neither these quantities nor the NaCl content varied systematically with pH. The hydrothermal products were dominated by a phase indexed on a primitive cubic cell ($a$ = 10.1175 Å) consistent with langbeinite-type $K_2Mn_2(SO_4)_3$; the reflections attributable to tetragonal $MnO_2$ coincide with those of this phase, so $MnO_2$ formation is not established. FE-SEM showed sheet- and flake-like features after the hydrothermal step, and EDS detected Ni, Mn, and O, but neither technique identifies the Mn-bearing phase. Over pH 8–11 the precursor pH is therefore not an effective processing variable: the retained by-products dominate the material, and purification, rather than pH, controls this route.

**Keywords**: *NiO; $MnO_2$; By-Product Retention; Precipitation; Hydrothermal Synthesis; Precursor pH; Microstructure*

## 1. INTRODUCTION

The demand for electrochemical energy-storage devices that deliver high power together with acceptable energy density has driven intense interest in supercapacitors. Among them, pseudocapacitors store charge through fast and reversible faradaic redox reactions at or near the electrode surface, rather than only through electrostatic adsorption at the electrode/electrolyte interface as in electrical double-layer capacitors. Transition-metal oxides are among the most widely studied pseudocapacitive electrode materials because they can provide high specific capacitance at relatively low cost compared with carbon-based materials [1,2].

Manganese dioxide ($MnO_2$) has attracted particular attention because of its low cost, natural abundance, environmental compatibility, and large theoretical capacitance (~1370 F/g) [2,3]. Its charge storage is highly sensitive to crystal structure, and the electrochemical response differs markedly among the $\alpha$-, $\beta$-, $\delta$-, and ramsdellite polymorphs and across the transitions between them [4,5]. $MnO_2$ nanostructures for supercapacitors have been produced by hydrothermal and microwave-assisted hydrothermal routes [6,7], and are frequently combined with conductive carbons to offset the intrinsically poor electrical conductivity of $MnO_2$ [8,9]; even the hydrothermal temperature alone strongly influences the resulting structure and capacitance [10].

Nickel oxide (NiO) is likewise promising, owing to its high theoretical capacitance, well-defined redox activity, and chemical stability [11,12,13]. A wide range of NiO nanostructures—flower-, sheet-, mesoporous- and skein-like—has been obtained by precipitation, sol–gel, and hydrothermal routes and evaluated as pseudocapacitor electrodes [14,15,16,17,18,19], often after compositing with carbon or a second oxide to raise the conductivity and rate capability [20,21,22,23]. NiO is also of interest beyond energy storage, for example as a *p*-type oxide semiconductor for gas sensing [24]. In practice, however, the low intrinsic conductivity of NiO and the structural degradation on repeated cycling limit the capacitance and stability actually achieved [11,12].

A widely adopted strategy to mitigate these limitations is to combine the two oxides into a NiO/$MnO_2$ nanocomposite, in which the phases act complementarily: a more conductive, redox-active framework supports the higher-capacitance phase and buffers the volume changes that cause degradation [12,25]. NiO/$MnO_2$ core/shell and related architectures prepared by hydrothermal routes have shown markedly improved electrochemical behaviour relative to the single oxides [11,26,27], and the same core/shell concept has proved effective for other transition-metal-oxide couples built on spinel $NiCo_2O_4$ [28] and on $Co_3O_4$/$MnO_2$ and $NiCo_2O_4$/$MnO_2$



© 2026 The Authors
This article is licensed under CC-BY 4.0
Open Access

composites [29,30,31,32,33,34].

The hydrothermal method is well suited to building such composites because the reaction temperature, time, and solution chemistry strongly influence the crystal structure and morphology of the product [35,36], allowing one oxide to be grown directly on a pre-formed second phase [37]. It has been used to tune the aspect ratio and shape of oxide nanostructures [38,39,40] and, in the present authors' group, to grow ZnO and $CeO_2$/ZnO for photocatalysis [41,42,43], ZnAl layered double hydroxides for dye adsorption [44], and $MnO_2$ and Mo-doped $Nb_2O_5$ electrodes for supercapacitors [10,45].

The phase content, crystallite size, defect density, and morphology of the composite are all established during synthesis—by the calcination or annealing step [46,47] as much as by the solution chemistry—and for the precipitation of oxides the precursor solution is a key handle on them [48,49,50]. In particular, the solution pH and precursor concentration set the degree of supersaturation and therefore the balance between nucleation and crystal growth that determines the final crystallite size [51,52,53]. Consistent with this, the pH during sol–gel or precipitation synthesis has been shown to change the phase, crystallite size, and morphology of $TiO_2$, $Fe_3O_4$, and ZnO [54,55,56,57], and the precursor molarity similarly shifts the properties of solution-grown ZnO [58,59,60]; the solution pH also alters the aggregation and dispersion state of already-formed NiO particles [61]. Despite this body of work, whether the precursor pH actually controls the crystallite size, defect content, and morphology of the *derived* NiO/$MnO_2$ nanocomposite—rather than only those of the bare oxide—has received limited attention.

Because these microstructural attributes govern electrode performance, they must be quantified reliably from the diffraction data. X-ray line-profile analysis yields the crystallite size and lattice microstrain from the peak broadening: the single-peak Scherrer estimate and the multi-peak Williamson–Hall and size–strain-plot methods, which separate the size and strain contributions, have been applied extensively to oxide nanomaterials such as ZnO, $TiO_2$, $Y_2O_3$, and spinel oxides [62,63,64,65,66,67,68], and are complemented by dislocation-density and lattice-parameter analyses [69]. Such careful structural characterization, as routinely reported for doped-oxide materials [70,71,72,73], is a prerequisite for interpreting how a synthesis variable such as pH acts on the material.

In this study, NiO nanoparticles were synthesized at four precursor pH values (8, 9, 10, and 11), subjected to a hydrothermal $MnO_2$-growth step, and characterized by X-ray diffraction (XRD), field-emission scanning electron microscopy (FE-SEM), and energy-dispersive X-ray spectroscopy (EDS) in order to test how far, and in what way, the precursor pH influences the phase content, microstructure, and morphology of the resulting material. Electrochemical evaluation is beyond the scope of the present work, which aims to establish the phase, microstructure, and morphology relationships on which any subsequent device testing of a purified composite must build.

## 2. EXPERIMENTAL DETAILS

### 2.1 Materials

Nickel(II) chloride hexahydrate ($NiCl_2{\cdot}6H_2O$), manganese(II) sulfate monohydrate ($MnSO_4{\cdot}H_2O$), potassium peroxodisulfate ($K_2S_2O_8$), sulfuric acid ($H_2SO_4$, 95–97%), sodium hydroxide (NaOH), distilled water, and deionized water were used as received.

### 2.2 Synthesis of NiO Nanoparticles (Precipitation)

NiO nanoparticles were prepared by precipitation. A 10 M NaOH solution was prepared by dissolving 4.000 g of NaOH in 10 mL of distilled water. Separately, 11.883 g of $NiCl_2{\cdot}6H_2O$ (0.2 M) was dissolved in 250 mL of distilled water on a hot plate at 50 °C under stirring. The NaOH solution was then added dropwise while the pH was monitored until the target value was reached; four precursor pH values were prepared—pH 8, 9, 10, and 11. The solution was held on the hot plate for 40 min, after which the green precipitate was separated by filtration through a poly(vinylidene fluoride) (PVDF) membrane filter and washed on the filter with deionized water until the filtrate reached neutral pH, and dried in an oven at 60 °C for 14 h. The dried solid was ground into a powder and calcined at 500 °C for 2 h.

The pH was brought to the target value by dropwise addition and was not controlled thereafter: no buffer or pH-stat was used, and because the precipitation of $Ni(OH)_2$ consumes $OH^-$, the pH will have drifted downward over the 40 min hold. The washing end-point was the neutrality of the filtrate; the number of washes was therefore not fixed but set by that criterion. This criterion tracks the removal of excess hydroxide, not of chloride: NaCl is a neutral salt and does not change the pH of the filtrate, so a neutral filtrate does not indicate that the NaCl has been removed. No chloride test (e.g. with $AgNO_3$) or conductivity measurement of the filtrate was made. One batch was prepared at each precursor pH and the syntheses were not independently repeated; one diffraction pattern was collected per sample. The uncertainties reported throughout are accordingly those of the profile fits and of the regressions—measurement and fitting precision—and do not include batch-to-batch reproducibility.

### 2.3 Hydrothermal $MnO_2$-Growth Step

To prepare the $MnO_2$ precursor solution, 1.352 g of $MnSO_4{\cdot}H_2O$ (0.2 M) and 2.163 g of $K_2S_2O_8$ (0.2 M) were weighed, 2 mL of $H_2SO_4$ was added, and the mixture was dissolved in 40 mL of distilled water and stirred at 600 rpm at room temperature until homogeneous. Then 1 g of the calcined NiO powder was added and stirred for 1 h at room temperature. The mixture was transferred to an autoclave and held at 120 °C for 8 h. The resulting precipitate was dried at 80 °C for 8 h, ground into a powder, and calcined at 500 °C for 2 h. This step was intended to yield a NiO/$MnO_2$ composite; because the phase analysis of Section 3.1 does not establish $MnO_2$, its product is referred to below as the *hydrothermal product*. The overall two-stage synthesis route is summarized in Fig. 1.

### 2.4 Characterization

Phase composition and crystallite size were determined using a PANalytical X'Pert$^3$ Powder diffractometer (Cu K$\alpha$, $\lambda$ = 0.15406 nm). The pH 8 powders were measured over $2\theta$ = 10–100° with a 0.05° step and a counting time of 31 s per step, whereas the pH 9–11 powders were measured over 5–80° with a 0.01° step and 1 s per step. The two protocols differ in sampling rather than in quality: the pH 8 scan has the better counting statistics per point (31 s against 1 s) but samples each reflection about five times more coarsely, so that a reflection of FWHM ~0.4° is spanned by some 8 points rather than some 40. The derived quantities are affected very unevenly,

© 2026 The Authors | CC-BY 4.0

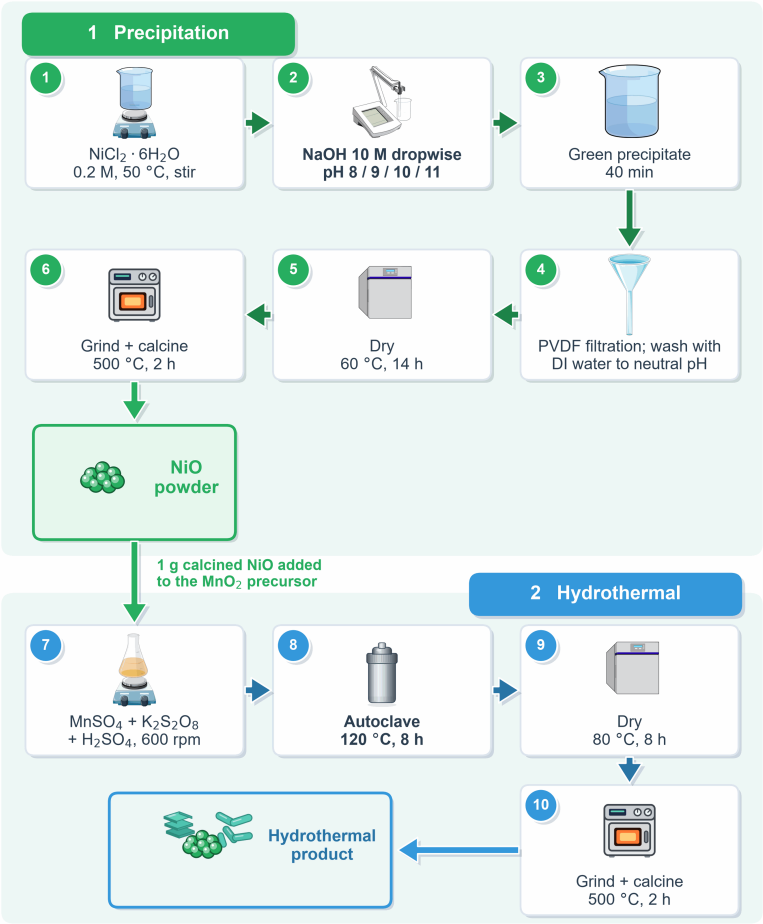


**Figure 1.** Schematic of the two-stage synthesis route: (1) precipitation of NiO at precursor pH 8–11 (steps 1–6), followed by (2) hydrothermal $MnO_2$-growth step (intended NiO/$MnO_2$ composite) at 120 °C for 8 h (steps 7–10). Selected equipment icons are from Bioicons (bioicons.com): hotplate stirrer and funnel by Servier (smart.servier.com, CC BY 3.0) and pH meter by DBCLS (CC BY 4.0); the remaining icons are in the public domain (CC0).

and we therefore compare them on the following basis. Quantities obtained from the peak *width* ($D$, $\varepsilon$) depend on how well the profile is sampled and are compared only across the identically measured pH 9–11 samples; the pH 8 values are reported for completeness but are excluded from the trend discussion. Quantities obtained from the peak *position* (the Nelson–Riley lattice parameter) are insensitive to the step size at this resolution, and quantities obtained from *intensity ratios measured within a single pattern* (the reference-intensity-ratio estimate and the texture coefficients) are likewise insensitive, because both phases are recorded in the same scan and the acquisition factors cancel in the ratio; the pH 8 sample is retained for both. Surface morphology was examined with a Thermo Scientific Quattro S field-emission scanning electron microscope at 15 kV, and elemental composition was obtained from energy-dispersive X-ray spectroscopy (EDS) map-sum spectra acquired in the same instrument. For the pH-8 samples, EDS elemental maps and point spectra were additionally acquired (at 20 kV) to resolve the spatial distribution of the by-product elements. Electron microscopy was performed only on the pH 8 and pH 9 samples; no FE-SEM or EDS data were acquired for the pH 10 and pH 11 powders or their hydrothermal products, and the two sessions differ in accelerating voltage, so the pH 8 and pH 9 micrographs are compared qualitatively only. Particle/cluster sizes were estimated from the 100 000× micrographs (2.70 nm per pixel, from the instrument metadata) by watershed segmentation (scikit-image; contrast-limited equalization, Gaussian smoothing, Otsu thresholding, and a distance-transform watershed), the size of each feature being reported as its equivalent circle diameter; because the material is agglomerated, these are semi-quantitative feature sizes rather than primary-particle diameters.

Each NiO reflection was fitted with a pseudo-Voigt profile on a locally linear background by non-linear least squares (SciPy) to extract the peak position $2\theta$ and the full width at half maximum $\beta$ (in radians). The cubic lattice parameter was obtained from the interplanar spacing of each reflection, $a = d_{hkl}\sqrt{h^2+k^2+l^2}$, and refined to $a_0$ by a Nelson–Riley extrapolation [74] of $a$ against $F(\theta) = \frac{1}{2}\left(\cos^2\theta/\sin\theta + \cos^2\theta/\theta\right)$ to $\theta$=90°. The crystallite size $D$ was first estimated from the NiO (200) reflection (~43.3°) with the Scherrer equation [75],

$$D = \frac{K\lambda}{\beta\cos\theta}, \qquad \delta = \frac{1}{D^2}, \qquad \varepsilon = \frac{\beta}{4\tan\theta}, \tag{1}$$

with $K$ = 0.9, where $\delta$ is the dislocation density and $\varepsilon$ the microstrain (the single-peak $\delta$ and $\varepsilon$ are nominal, as each ascribes the whole broadening to a single source). Because

© 2026 The Authors | CC-BY 4.0

the single-peak Scherrer analysis assigns all broadening to size, the size and strain contributions were separated with two multi-peak methods applied to the four NiO reflections that are free of NaCl overlap—(111), (200), (220), and (222); the (311) reflection was excluded as it coincides with NaCl (420). The Williamson–Hall uniform deformation model [76],

$$\beta \cos\theta = \frac{K\lambda}{D} + 4\varepsilon \sin\theta, \tag{2}$$

yields $D$ from the intercept and $\varepsilon$ from the slope of $\beta \cos\theta$ against 4 $\sin\theta$, whereas the size–strain plot [63,68]

$$(d_{hkl}\,\beta\cos\theta)^2 = \frac{K\lambda}{D}\left(d_{hkl}^2\,\beta\cos\theta\right) + \left(\frac{\varepsilon}{2}\right)^2 \tag{3}$$

yields $D$ from the slope and $\varepsilon$ from the intercept. Standard errors for all derived quantities were propagated from the covariance matrices of the profile fits and of the Nelson–Riley, Williamson–Hall, and size–strain-plot regressions. No instrumental-broadening standard was measured and the raw data retain the Cu K$\alpha_2$ component, so the reported $D$ and $\varepsilon$ are apparent values; the comparison across the identically measured pH 9–11 samples is more robust than the absolute magnitudes.

The relative amount of NaCl was estimated from the integrated (200) intensities of NiO and NaCl by the reference-intensity-ratio method [77], using reference intensities $R = m|F|^2\,\mathrm{LP}/V^2$ computed from the rock-salt structures with Cromer–Mann atomic form factors and the Lorentz–polarization factor (a two-phase NiO+NaCl assumption, with no microabsorption correction, so the result is semi-quantitative). The NiO texture was assessed from the coefficient [78] $\mathrm{TC}(hkl) = [I(hkl)/R(hkl)]/\langle I/R\rangle$, which equals unity for a randomly oriented powder.

## 3. RESULTS AND DISCUSSION

### 3.1 XRD Analysis

Figure 2a shows the XRD patterns of the NiO powders prepared at precursor pH 8–11. The diffraction peaks at $2\theta \approx 37.2$, 43.3, 62.9, 75.4, and 79.4°, indexed to the (111), (200), (220), (311), and (222) planes, confirm the formation of cubic NiO (PDF 00-073-0450). Additional reflections at $2\theta \approx 27$, 31.7, 45.4, and 56.4° correspond to a cubic halite (NaCl) phase (PDF 00-005-0628). This by-product forms during precipitation according to $NiCl_2 + 2NaOH \rightarrow Ni(OH)_2\downarrow + 2NaCl$; the $Ni(OH)_2$ then dehydrates to NiO during calcination. This NaCl is a major crystalline component of the powders rather than a trace impurity: for the pH 9–11 samples the NaCl (200) reflection at ~31.6° is the most intense peak in the whole pattern, and its intensity relative to NiO varies non-monotonically with pH—largest at pH 9 and comparable at pH 10–11 (a semi-quantitative weight fraction for all four samples, including pH 8, is given below, together with the reason why this intensity-ratio quantity, unlike the width-derived ones, can be compared across the two acquisition protocols). The persistence of this strong NaCl signal shows that the washing step did not remove the chloride/sodium by-product.

Figure 2b shows the XRD patterns of the hydrothermal products. The NiO (111) reflection at $2\theta \approx 37°$ is retained. The patterns are otherwise dominated by a single by-product phase. Eleven of the resolved reflections index on one primitive cubic cell, refined to $a$ = 10.1175 Å with a root-mean-square deviation of 0.068° in $2\theta$ and ten of the eleven matched to within 0.06° (Table 1). The strong reflection near 28° is the (310) reflection of this cell, which is the strongest reflection of the langbeinite structure type. Both the cell size and the $K_2S_2O_8/H_2SO_4/MnSO_4$ reagent chemistry, followed by calcination at 500 °C, point to a langbeinite-type potassium–manganese sulfate of the $K_2Mn_2(SO_4)_3$ type: the refined cell agrees to within 0.03% with the reference value for synthetic cubic $K_2Mn_2(SO_4)_3$ ($a$ = 10.1143 Å, space group $P2_13$ [79]), and it is clearly distinct from the Ni-langbeinite $K_2Ni_2(SO_4)_3$ ($a$ = 9.8436 Å [79]). Because substitution of the smaller $Ni^{2+}$ would contract the cell, the agreement also suggests that little nickel is incorporated in this phase. One weak reflection at 24.11° (~5% relative intensity) remains unindexed, and a definitive assignment would still require whole-pattern (Rietveld) refinement or a complementary technique, so this is presented as an indexing result rather than a completed phase identification.

**Table 1.** Indexing of the dominant by-product reflections of the hydrothermal product (pH 9) on a primitive cubic cell refined to $a$ = 10.1175 Å (r.m.s. deviation 0.068° in $2\theta$). Intensities are peak heights relative to the strongest reflection. A weak reflection at 24.11° (~5%) is not indexed by this cell.

| $2\theta_{obs}$ (°) | $I/I_0$ (%) | $hkl$ | $2\theta_{calc}-2\theta_{obs}$ (°) |
|---|---|---|---|
| 15.14 | 12 | (111) | +0.02 |
| 19.61 | 9 | (210) | −0.01 |
| 21.50 | 16 | (211) | 0.00 |
| 24.67 | 13 | (220) | +0.20 |
| 26.43 | 4 | (221) | −0.02 |
| 27.90 | 100 | (310) | −0.04 |
| 29.30 | 12 | (311) | −0.05 |
| 31.91 | 6 | (320) | −0.04 |
| 33.16 | 43 | (321) | −0.06 |
| 36.57 | 32 | (410) | +0.02 |
| 41.83 | 8 | (332) | +0.02 |

The indexing bears directly on the assignment of $MnO_2$. The evidence for tetragonal $MnO_2$ consisted of two reflections, measured at 45.78° and 56.12°. The cubic cell above generates reflections at 45.69° and 55.98°, against 46.10° and 56.66° for tetragonal $MnO_2$ (PDF 01-072-0071), so the by-product cell fits these two positions at least as well. We do not read that as positive evidence for the sulfate at those positions, because a cubic cell of this size generates a dense set of reflections above 45° and coincidental agreement is likely; the conclusion that follows is the weaker and safer one, that the presence of $MnO_2$ is not established by these two reflections alone. The third expected $MnO_2$ reflection, near 37°, overlaps NiO (111) and cannot be resolved. Because the sulfate is itself Mn-bearing, the detection of Mn by EDS (Section 3.3) does not settle the question either. We therefore describe the hydrothermal product as a multiphase, NiO-bearing powder in which $MnO_2$ is the intended but unconfirmed Mn-bearing phase.

The weak NiO signal is consistent with dilution by these by-product phases and with the low overall crystallinity of the hydrothermal-product patterns. Beyond the single-peak Scherrer estimate, the microstructure of the NiO powders was analysed by refining the cubic lattice parameter and by separating the size and strain contributions to the broadening with the Williamson–Hall and size–strain-plot methods; the results are collected in Table 2.

The Nelson–Riley refined lattice parameter is $a_0$ = 4.178 Å (individual values 4.1771–4.1781 Å; Table 2) for all four

© 2026 The Authors | CC-BY 4.0

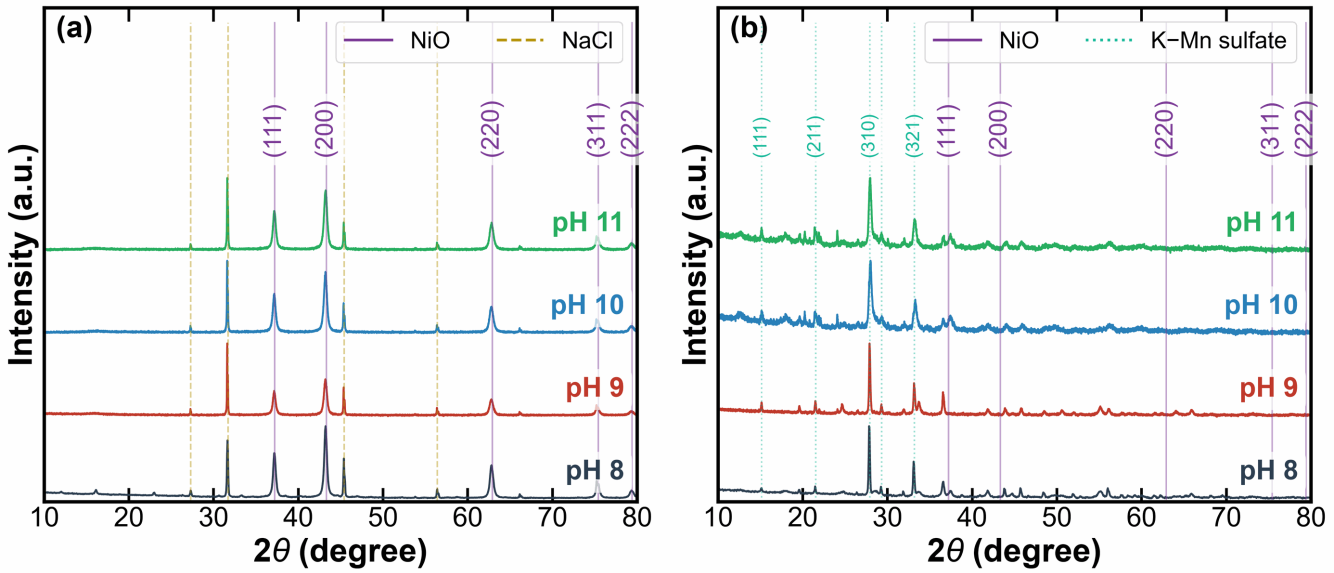


**Figure 2.** XRD patterns of the samples synthesized at precursor pH 8–11: (a) NiO powders, with the cubic NiO and NaCl reflections marked; and (b) the products of the hydrothermal step, with the NiO reflections marked and the reflections of the langbeinite-type by-product phase indexed in Table 1.

**Table 2.** Microstructure of the NiO powders from XRD: Nelson–Riley lattice parameter $a_0$, and crystallite size $D$ and microstrain $\varepsilon$ from the single-peak Scherrer (NiO (200)), Williamson–Hall (W–H), and size–strain-plot (SSP) analyses. Figures in parentheses are standard errors in units of the last quoted digit; they are the standard errors of the profile fits and of the regressions, with one batch and one diffraction pattern per condition, and do not include batch-to-batch reproducibility. The pH 8 values are reported for completeness but were acquired under a different protocol and are not directly comparable with those for pH 9–11 (Section 2).

| Sample | $a_0$ (Å) | $D_{Sch}$ (nm) | $D_{WH}$ (nm) | $\varepsilon_{WH}$ ($10^{-3}$) | $D_{SSP}$ (nm) | $\varepsilon_{SSP}$ ($10^{-3}$) |
|---|---|---|---|---|---|---|
| pH 8 | 4.1771(2) | 23.4(1) | 32.9(29) | 1.30(19) | 26.4(15) | 0.98(15) |
| pH 9 | 4.1781(8) | 20.0(1) | 31.0(15) | 1.58(11) | 25.5(12) | 1.26(10) |
| pH 10 | 4.1778(8) | 19.7(1) | 29.5(5) | 1.56(4) | 24.4(5) | 1.25(5) |
| pH 11 | 4.1775(6) | 19.6(1) | 25.2(25) | 1.08(28) | 22.7(11) | 1.06(15) |

precursor pH values (Fig. 3c), equal to the bulk NiO value (4.1769 Å) within uncertainty and without a systematic dependence on pH. The macrostrain (unit-cell dilation, $\Delta a/a \approx 0$) is therefore negligible—distinct from the non-zero microstrain ($\sim 1\times10^{-3}$) obtained below from line broadening—so the precursor pH does not distort the NiO lattice. The three size estimates agree in magnitude: the single-peak Scherrer value (NiO (200)) is 20–23 nm, the Williamson–Hall value 25–33 nm, and the size–strain-plot value 23–26 nm (Fig. 3a). The offset between the single-peak and multi-peak sizes reflects the microstrain ($\sim 1\times10^{-3}$; Fig. 3b) that the single-peak Scherrer analysis otherwise attributes to size. Across the identically measured pH 9–11 series the pH-to-pH variations in both $D$ and $a_0$ are comparable to their standard errors (Table 2, Fig. 3); the apparent decrease of the four-peak Williamson–Hall size at pH 11 (Fig. 4d) is, moreover, an artefact of the weak high-angle (222) reflection and disappears (~30 nm, constant within error) once that reflection is excluded. The NiO crystallite size therefore shows no systematic dependence on precursor pH and stays of the order of 20–30 nm, consistent with the pH-insensitive lattice parameter and of the same order as NiO nanoparticle sizes reported for related precipitation syntheses [13,18]. This robustness contrasts with reports in which the precursor pH markedly altered the phase, size, or morphology of other precipitated oxides such as $TiO_2$, $Fe_3O_4$, and ZnO [54,55,56], and indicates that, over the pH 8–11 range studied, the NiO microstructure is comparatively insensitive to this parameter.

Why the precursor pH should have so little effect over this window is worth setting out, since the contrast with those oxides is otherwise puzzling. Four factors act in the same direction. First, the window lies entirely above the completion of precipitation: for 0.2 M $Ni^{2+}$ and $K_{sp}(Ni(OH)_2) \approx 5.5\times10^{-16}$, precipitation begins near pH 6.7 and is more than 99.7% complete by pH 8 [80]. The four endpoints therefore differ in residual $Ni^{2+}$ by orders of magnitude, but all correspond to essentially complete precipitation. Second, nucleation is governed by local rather than bulk supersaturation: 10 M NaOH was added dropwise into 0.2 M $NiCl_2$, so that the supersaturation at the point of contact is extreme and much the same in all four syntheses, and the bulk endpoint pH is reached only once the nucleation burst is over. Third, $Ni^{2+}$ is not amphoteric in this window. The systems in which the precursor pH strongly alters the product—$TiO_2$, $Fe_3O_4$, ZnO—involve either a phase selection or a soluble hydroxo-complex equilibrium, $Zn(OH)_2$ in particular redissolving as hydroxozincate complexes at high pH [81]; $Ni(OH)_2$ has no competing phase and no soluble complex between pH 8 and 11, so there is no chemical lever for the pH to act on. Fourth, the calcination at 500 °C for 2 h largely resets the microstructure, so that

© 2026 The Authors | CC-BY 4.0

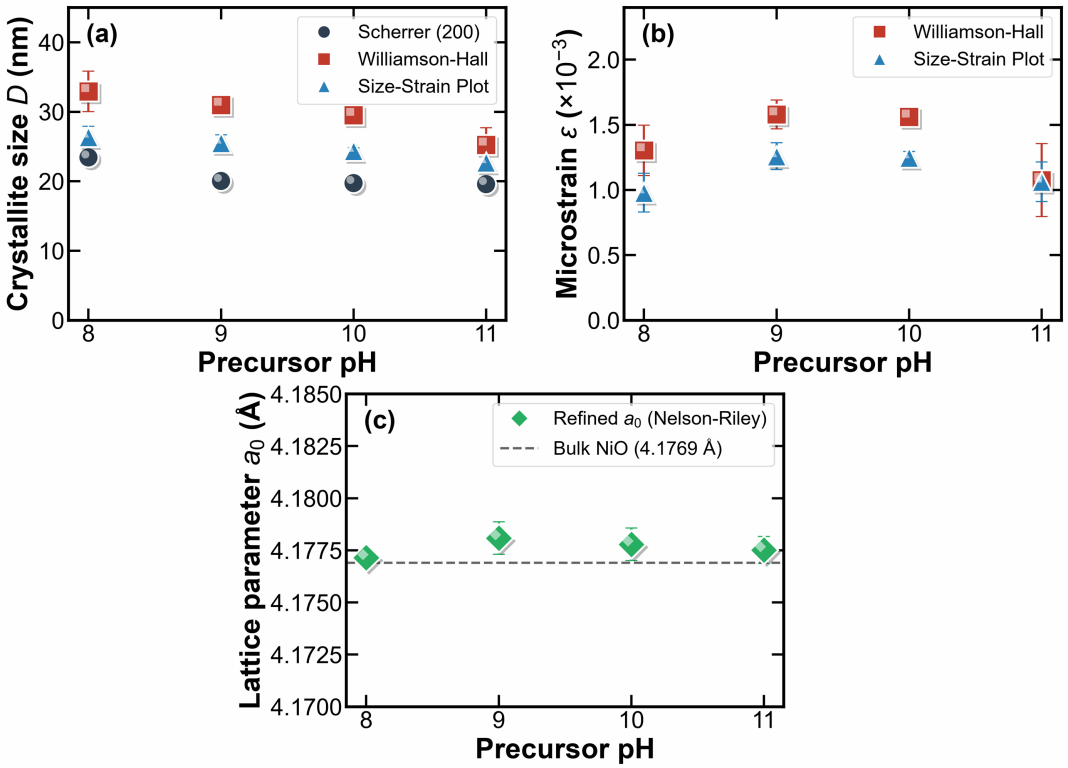


**Figure 3.** Microstructure of the NiO powders as a function of precursor pH: (a) crystallite size $D$ from the Scherrer, Williamson–Hall, and size–strain-plot methods; (b) microstrain $\varepsilon$ from the Williamson–Hall and size–strain-plot methods; and (c) the Nelson–Riley refined lattice parameter $a_0$, with the bulk NiO value shown for reference.

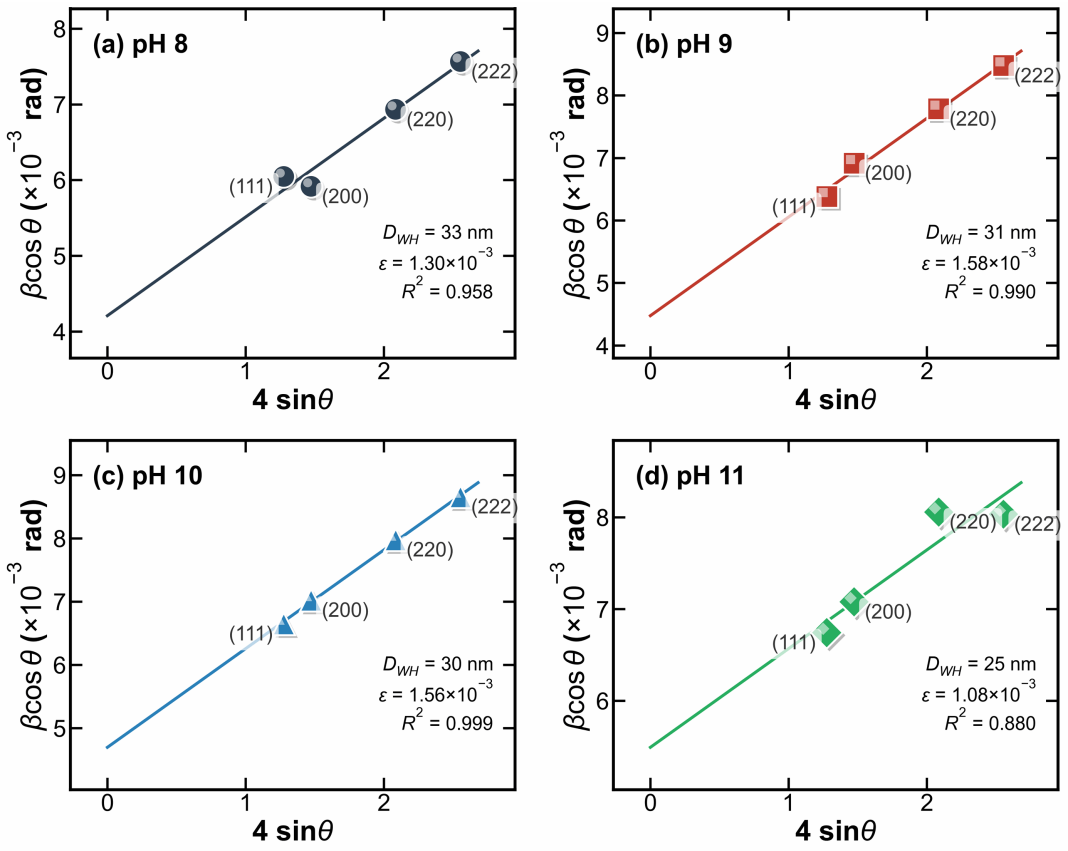


**Figure 4.** Williamson–Hall plots ($\beta \cos \theta$ versus 4 sin $\theta$) for the NiO powders at precursor pH (a) 8, (b) 9, (c) 10, and (d) 11, using the (111), (200), (220), and (222) reflections. The fitted crystallite size $D_{WH}$, microstrain $\varepsilon$, and $R^2$ are annotated in each panel.

© 2026 The Authors | CC-BY 4.0

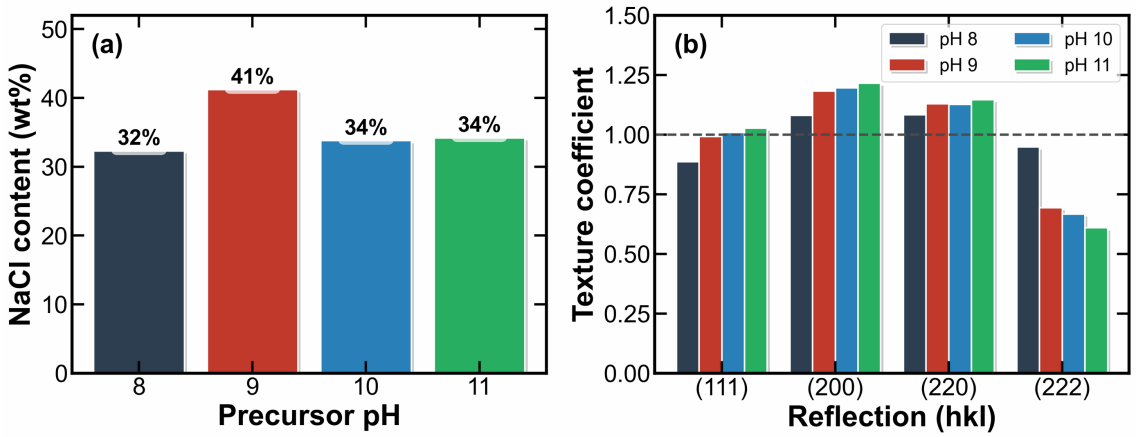


**Figure 5.** (a) Semi-quantitative NaCl content of the NiO powders (reference-intensity-ratio method, (200) reflections) as a function of precursor pH; and (b) NiO texture coefficients for the (111), (200), (220), and (222) reflections (dashed line: randomly oriented powder, TC=1).

the final crystallite size reflects the solid-state step rather than the as-precipitated hydroxide. Taken together, these indicate that pH 8–11 is a plateau, and that a pH effect in this system would have to be sought below the completion of precipitation or, for the by-product content, in the washing step rather than in the precipitation itself. Two further checks reinforce this picture. First, a reference-intensity-ratio estimate from the (200) reflections puts the NaCl content of the powders at 32–41 wt% (Fig. 5a), confirming quantitatively that the by-product is a major fraction of the crystalline material. The individual values are 32, 41, 34 and 34 wt% at pH 8, 9, 10 and 11 respectively: the content is largest at pH 9 and does not vary monotonically with pH. Because this estimate is a ratio of integrated intensities of two phases recorded in the same scan, the acquisition conditions cancel, and the pH 8 sample is therefore included here on the same footing as the others, unlike the width-derived quantities of Table 2.

The estimate is semi-quantitative and its limitations should be stated. It assumes a two-phase NiO+NaCl mixture, so that any amorphous or unindexed material is ignored and both phases are over-weighted in proportion; the reference intensities are computed from the rock-salt structures rather than measured against a standard; no microabsorption correction is applied, although the linear attenuation coefficients of the two phases differ appreciably at Cu K$\alpha$; and the Cu K$\alpha_2$ component is not stripped. Microabsorption should be minor for the NiO, whose features lie well below the scale at which the Brindley correction becomes significant, but it cannot be excluded for the NaCl, whose grain size after drying is not known. Fluorescence does not contribute, since the Ni K edge (8.33 keV) lies above Cu K$\alpha$ (8.04 keV). We therefore attach an uncertainty of order 5 wt% absolute to these values, and use them only to establish that NaCl is a major crystalline component, not to assign a precise weight fraction or a pH trend.

An independent cross-check supports the magnitude. The 0.05 mol of $NiCl_2{\cdot}6H_2O$ charged yields at most 0.1 mol of NaCl (5.84 g) alongside 0.05 mol of NiO (3.73 g), that is 61 wt% NaCl if none were removed. The measured 32–41 wt% therefore corresponds to the washing step having removed 56–70% of the NaCl formed, a physically sensible figure obtained without reference to the diffraction analysis.

Second, the NiO texture coefficients (Fig. 5b) lie close to unity (0.9–1.2 for the strong (111), (200), and (220) reflections), showing that the NiO is essentially randomly oriented; this validates the random-orientation assumption underlying the intensity-based size and phase analyses. The lower value for the weak (222) reflection reflects its poor counting statistics rather than genuine texture. For the hydrothermal products a reliable crystallite size could not be obtained. The hydrothermal-product patterns are weak (maximum intensity 1600–3400 counts, against ~6500 counts for the NiO powders), and in the NiO (200) region the signal-to-noise ratio is only 1.4–1.7. Moreover, the strongest feature in this region lies at 43.8–44.1°—at the by-product phases, consistent with the (422) reflection of the cubic cell of Table 1, calculated at 43.80°—rather than at the NiO (200) position (43.3°). Figure 6 compares the hydrothermal-product and NiO-powder patterns over 40–48° and shows that the sharp NiO (200) reflection of the powder has no counterpart in the hydrothermal product. A single-peak fit in this window therefore characterizes a secondary phase, not NiO, and no NiO crystallite size is reported for the hydrothermal products. The much lower peak intensities and higher relative background of the hydrothermal-product patterns further indicate that the hydrothermal products are considerably less crystalline than the NiO powders, which would be consistent with a poorly crystalline Mn-bearing phase, although that phase is not identified here. The dominance of the NaCl and sulfate by-products in the diffraction patterns underlines that improved washing and purification are the priority for future work.

### 3.2 FE-SEM Analysis

Figure 7 compares the morphology of the NiO powder and the hydrothermal product for a representative sample (pH 9 precursor). The NiO powder (Fig. 7a) consists of agglomerated, approximately spherical nanoclusters formed by the coalescence of smaller grains [13], interspersed with occasional elongated rod- and fibre-like features. Because the EDS spectrum of this powder contains only Ni and O (Section 3.3), these elongated features are not a manganese phase; they are most plausibly $Ni(OH)_2$-derived NiO filaments retained through calcination, or thin fibres from the conductive sample mount. The clusters span tens to several hundred nanometres (quantified below), whereas the crystallite size from XRD is only 20–30 nm, so each cluster is a polycrystalline aggregate

© 2026 The Authors | CC-BY 4.0 

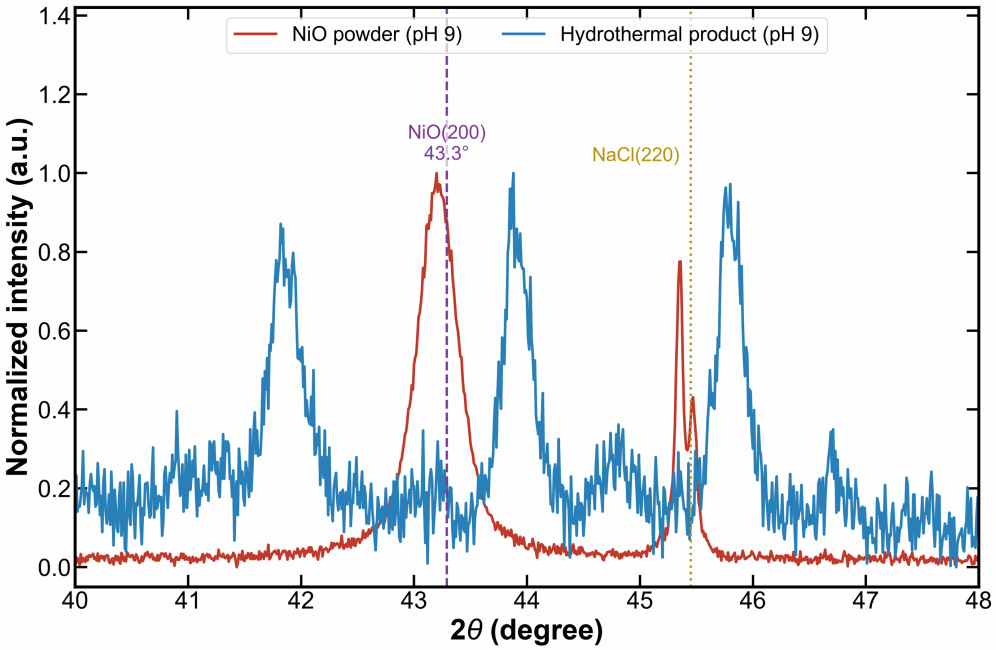


**Figure 6.** Comparison of the NiO powder and hydrothermal-product XRD patterns (pH 9) over 40–48°. The sharp NiO (200) reflection of the powder at 43.3° has no counterpart in the hydrothermal product, where the intensity near 43.3° is at noise level.

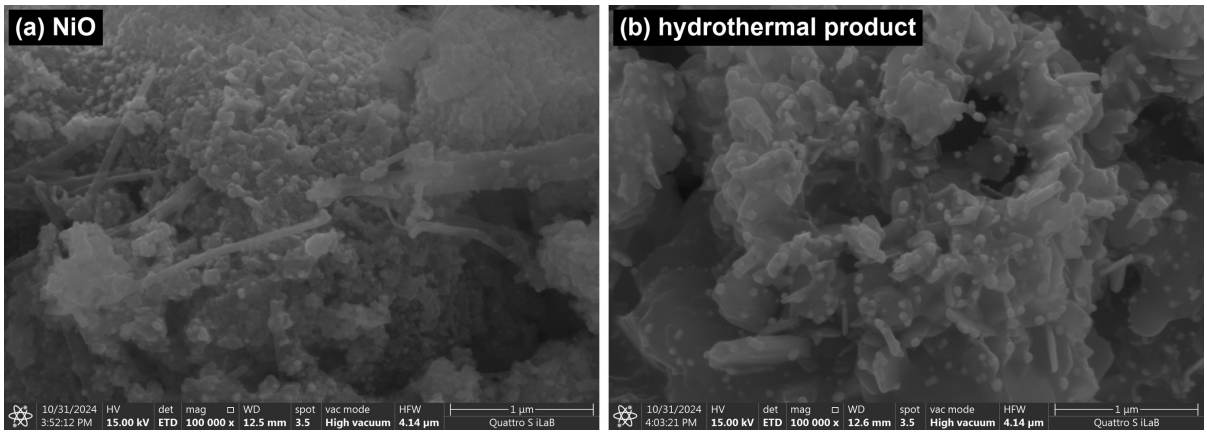


**Figure 7.** FE-SEM micrographs of the pH 9 samples: (a) NiO and (b) the hydrothermal product (100 000×).

of many NiO domains rather than a single crystal. Such agglomeration is characteristic of oxides obtained by hydroxide precipitation and calcination, in which capillary and surface forces during drying and solid-state coarsening during calcination draw the primary particles together.

After the hydrothermal step (Fig. 7b) the fine morphology changes: the product is dominated by sheet- and flake-like features carrying nodular particles, which are absent from the bare NiO powder. We describe these features without assigning them to a phase. Neither technique used here resolves the interfacial structure—FE-SEM because no cross-sections were prepared and only surface topography was imaged, and EDS because the map-sum spectra have no spatial resolution at the relevant scale—and, because the langbeinite-type sulfate of Section 3.1 is present in quantity and its habit under these conditions is not independently known, the morphology cannot distinguish it from $MnO_2$. Under the acidic hydrothermal conditions used here the peroxodisulfate would be expected to oxidize $Mn^{2+}$ to $MnO_2$ ($MnSO_4 + K_2S_2O_8 + 2H_2O \rightarrow MnO_2 + K_2SO_4 + 2H_2SO_4$), with the pre-formed NiO clusters acting as heterogeneous substrates for that growth and the morphology depending on the hydrothermal temperature and time [35]. The present data do not confirm that this is what occurred: as set out in Section 3.1, the dominant crystalline product of the hydrothermal step is a potassium–manganese sulfate, the reflections attributable to $MnO_2$ are not distinguishable from those of that phase, and EDS cannot say which phase hosts the manganese it detects. What can be said is that the product is an intimate multiphase mixture rather than the ordered, free-standing core/shell arrays reported for template- or foam-supported $NiO/MnO_2$ electrodes [11,12,25,34], and that elongated rod/fibre features are already present in the bare NiO, so that the morphology by itself is not diagnostic of composite formation. Because FE-SEM and EDS were acquired only for the pH 8 and pH 9 samples, they document the hydrothermal step at fixed precursor pH and are not, on their own, evidence for a dependence of morphology on that variable.

© 2026 The Authors | CC-BY 4.0 

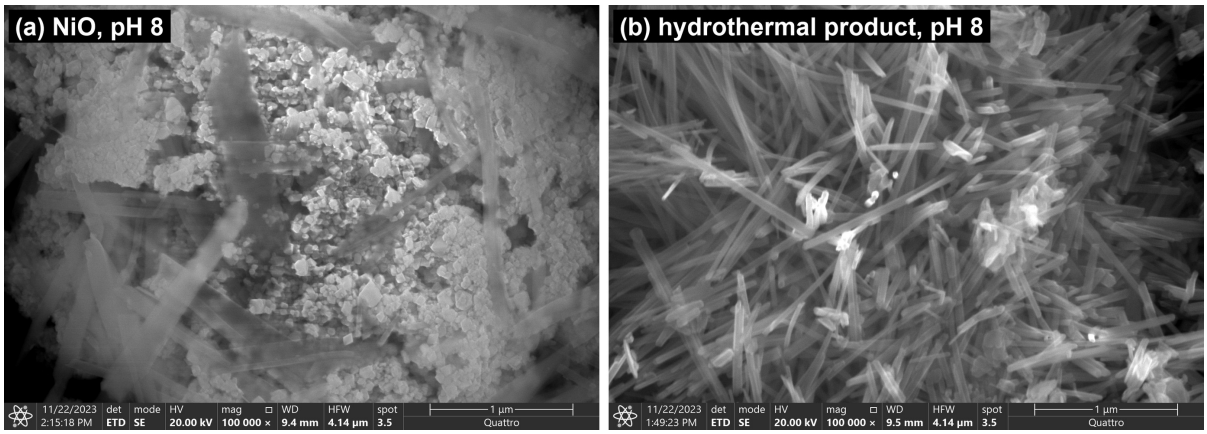


**Figure 8.** FE-SEM micrographs of the pH-8 samples (100 000×, 20 kV): (a) NiO powder and (b) the hydrothermal product. The instrument data bar, including the calibrated scale bar, is retained. These images were acquired in a different session from those of Fig. 7 and are compared with them qualitatively only.

Micrographs of the pH-8 samples (Fig. 8) are included for completeness, although they do not settle the question either. The pH-8 NiO powder (Fig. 8a) shows the same granular nanoparticles together with the elongated rod/fibre features already noted at pH 9, whereas the pH-8 hydrothermal product (Fig. 8b) is dominated by dense elongated needles rather than by the sheet- and flake-like features seen at pH 9. We do not read this difference as an effect of the precursor pH. The two sets were acquired in separate sessions at different accelerating voltages (20 kV for pH 8, 15 kV for pH 9); each is a single field of a strongly agglomerated and demonstrably heterogeneous powder (Section 3.3); and rod/fibre features are present in the bare NiO at both pH values, so they cannot be attributed to the hydrothermal step. XRD, which samples the bulk, finds the same dominant by-product phase at all four precursor pH values (Section 3.1) and gives no indication of a pH-driven change in phase content. These micrographs are therefore reported as documentation of the material rather than as evidence on the pH dependence of the morphology, which the present data cannot establish either way. A watershed segmentation of the 100 000× micrographs (Fig. 9) provides a semi-quantitative measure of the apparent particle/cluster size. The equivalent circle diameter has a median of 65 nm for the NiO powder ($n$=478) and 83 nm for the hydrothermal product ($n$=335), with broad, right-skewed distributions extending beyond 300 nm. Both medians greatly exceed the NiO crystallite size from XRD (20–30 nm), quantitatively confirming that the imaged particles are polycrystalline aggregates; the somewhat larger hydrothermal-product values are consistent with the sheet- and flake-like features formed in the hydrothermal step, whatever their phase. Because the particles are agglomerated, these values are approximate and represent feature or cluster sizes rather than primary-particle diameters.

### 3.3 EDS Analysis

The elemental composition obtained from the EDS map-sum spectra (pH 9 samples) is given in Table 3. The measurement is standardless and semi-quantitative, and light-element (oxygen) quantification is unreliable, so the metal ratios are more informative than the absolute oxygen contents. For the NiO powder, only Ni and O were detected, with a Ni-rich metal:oxygen ratio (Ni 55, O 45 at.%) consistent with NiO within EDS accuracy and with cubic NiO being the only Ni-bearing phase seen by XRD. No sodium or chlorine was detected, although NaCl is a major crystalline component of the bulk powder; the analysed field was therefore NiO-rich and not representative of the bulk, which is itself direct evidence of spatial heterogeneity.

**Table 3.** EDS composition of the pH 9 NiO powder and hydrothermal product from a single instrument map-sum spectrum. The values are standardless and semi-quantitative (single region); the oxygen content in particular is unreliable and should not be read as stoichiometry.

| Sample | Element | Weight (%) | Atomic (%) |
|---|---|---|---|
| NiO | Ni | 82 | 55 |
| NiO | O | 18 | 45 |
| Hydrothermal product | Mn | 43 | 26 |
| Hydrothermal product | O | 29 | 59 |
| Hydrothermal product | Ni | 28 | 16 |

For the hydrothermal product, Ni, Mn, and O were all detected, confirming that manganese is present in the analysed region, although, as noted in Section 3.1, EDS cannot establish which phase hosts it. The manganese content exceeds the nickel content (Mn:Ni ~1.6:1 by atom). This is not a consequence of manganese having been charged in excess. The 1.352 g of $MnSO_4{\cdot}H_2O$ corresponds to 8.00 mmol of Mn, whereas 1 g of the calcined powder, taken as pure NiO, corresponds to 13.39 mmol of Ni—a charged ratio of 0.60:1, that is, manganese in deficit. Correcting for the residual NaCl measured in that same powder (41 wt% at pH 9) lowers the nickel content to 7.90 mmol and raises the charged ratio to 1.01:1, or approximately equimolar. The measured 1.6:1 therefore exceeds the charged ratio, and we attribute the difference to the measurement rather than to the synthesis: the spectrum is a single map-sum over one field that is demonstrably unrepresentative, as the absence of K and S from it shows; EDS samples only the outermost micrometre, so that a Mn-bearing phase formed on the outside of the NiO clusters is over-weighted relative to the nickel it covers; and the quantification is standardless. We accordingly treat the Mn:Ni ratio as qualitative evidence that manganese is present, not as a measure of the amounts charged. No potassium or sulfur was detected in this map-sum spectrum,

© 2026 The Authors | CC-BY 4.0

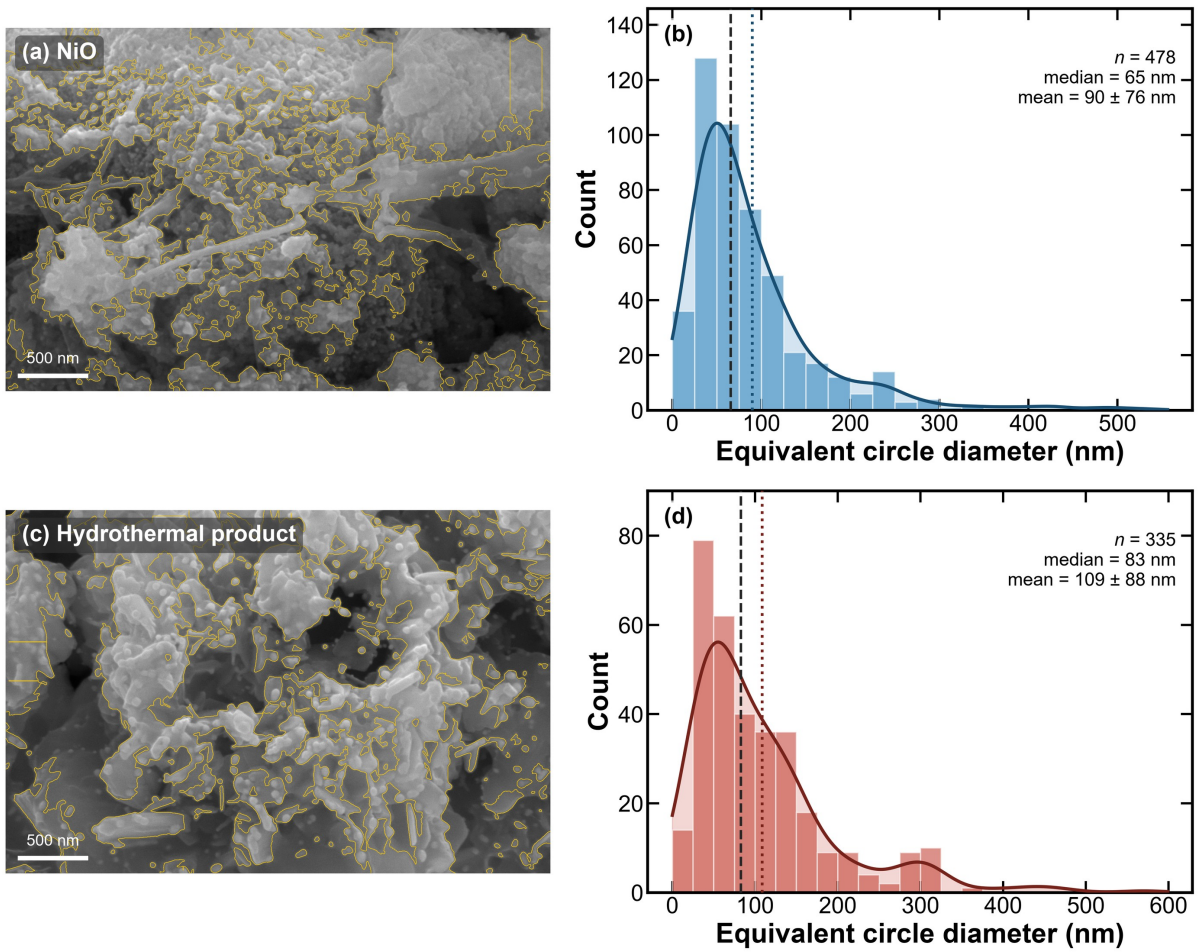


**Figure 9.** Watershed segmentation of the 100 000× FE-SEM micrographs (segmented features outlined in yellow) and the resulting equivalent-circle-diameter distributions for (a, b) the NiO powder and (c, d) the hydrothermal product; the smooth curve is a kernel-density estimate, and the dashed and dotted lines mark the median and mean, respectively. Values are semi-quantitative feature sizes (agglomerated material).

even though the hydrothermal-product diffraction pattern is dominated by potassium–manganese–sulfate by-products; as for the NiO powder, this reflects a single, non-representative analysis field rather than the absence of those phases. The oxygen content is over-estimated here (O 59 at.%) whereas it was under-estimated for the NiO powder, confirming that the EDS oxygen values cannot be read as stoichiometry in either sample; the metal ratio (Mn:Ni ~1.6:1) is the more robust output, and the analysis is best regarded as qualitative confirmation that manganese is present in the product.

The spatial character of the by-products was examined directly on the pH-8 samples. For the pH-8 hydrothermal product, elemental maps (Fig. 10) show Mn and O distributed across the whole field with Ni interspersed and—in contrast to the pH-9 map-sum spectrum—clear K and S signals, confirming that the potassium–manganese–sulfate by-products lie within the analysed region. Point spectra on the same sample bear out the heterogeneity: some regions contain about 11 at.% K and 13 at.% S (a sulfate-rich domain) whereas others show only Mn, O, and Ni; likewise, point spectra on the pH-8 NiO powder detect Na and Cl (residual NaCl) in some regions but not in others. The by-product phases seen by XRD are therefore real but spatially localized, which explains why a single map-sum field can miss them and confirms that the EDS analysis is representative only of the region sampled.

### 3.4 Growth Mechanism

The structural and compositional results are drawn together in the growth scheme of Fig. 11. In the precipitation stage, $Ni^{2+}$ and $OH^-$ form $Ni(OH)_2$ nuclei that grow, aggregate, and convert to cubic NiO on calcination, while the $Na^+$ and $Cl^-$ counter-ions crystallize into the NaCl by-product that survives the washing step (32–41 wt%; Section 3.1). Across pH 8–11 this sequence yields a NiO microstructure that is indistinguishable within the measurement uncertainty of a single batch per condition ($D \approx 20$–$30$ nm, $a_0 \approx 4.178$ Å), and a by-product content that varies non-monotonically, so that within this window the precursor pH acts on neither the oxide nor, systematically, on the amount of by-product. In the hydrothermal stage, $Mn^{2+}$ is expected to be oxidized by peroxodisulfate to $MnO_2$ ($Mn^{2+} + S_2O_8^{2-} + 2H_2O \rightarrow MnO_2 + 2SO_4^{2-} + 4H^+$), the classic persulfate route to $MnO_2$ nanostructures [82], alongside the pre-formed NiO. The observed product, however, is a multiphase, NiO-bearing powder whose crystalline fraction is dominated by a langbeinite-type potassium–manganese sulfate; whether $MnO_2$ is also present is not resolved by the present data (Section 3.1). Because neither the phases nor their spatial relationship are fully established, the scheme deliberately depicts coexisting

© 2026 The Authors | CC-BY 4.0

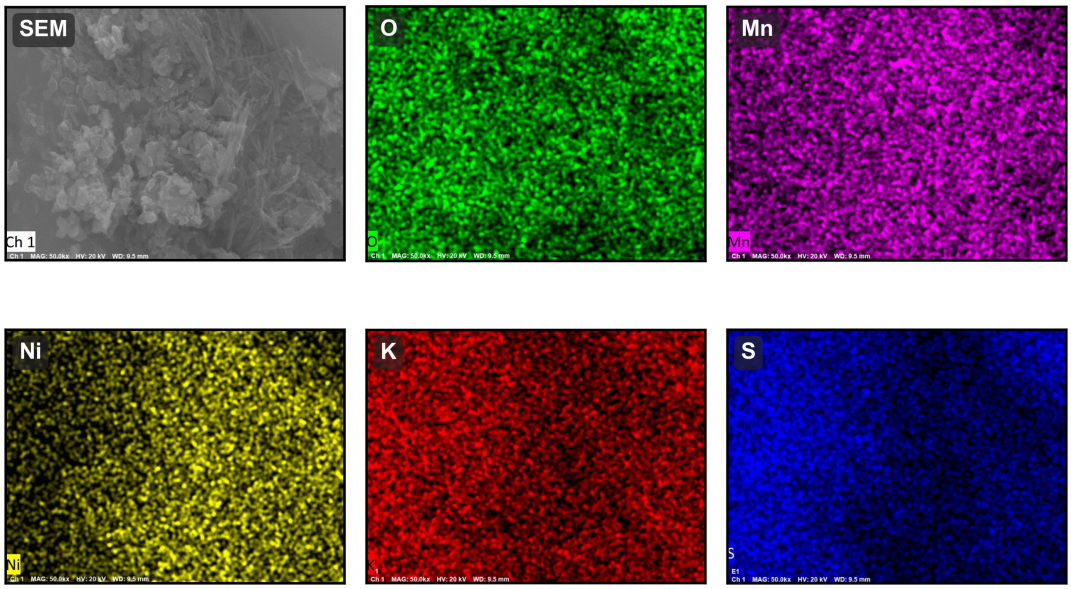


**Figure 10.** EDS elemental maps of the pH-8 hydrothermal product (50 000×): secondary-electron image (SEM) and the O, Mn, Ni, K, and S maps. Mn and O span the field with Ni interspersed, and K and S are both present—evidencing the potassium–manganese–sulfate by-product within the analysed region.

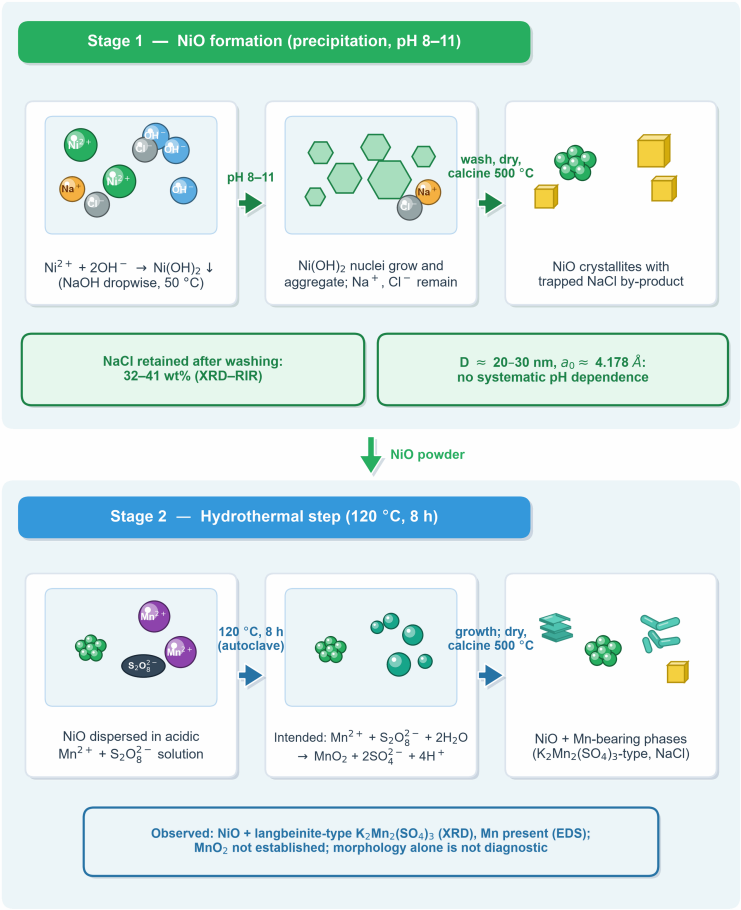


**Figure 11.** Proposed growth scheme. Stage 1 (precipitation, pH 8–11): $Ni(OH)_2$ nucleation and growth followed by calcination to NiO, with the NaCl by-product retained after washing (32–41 wt% by XRD–RIR); the NiO microstructure shows no systematic pH dependence. Stage 2 (hydrothermal, 120 °C, 8 h): peroxodisulfate oxidation of $Mn^{2+}$ is the intended route to $MnO_2$ alongside the pre-formed NiO, but the observed crystalline product is dominated by a langbeinite-type potassium–manganese sulfate and the presence of $MnO_2$ is not established (Section 3.1). The phases are drawn side by side because the data establish neither the full phase content nor the spatial arrangement.

© 2026 The Authors | CC-BY 4.0 

phases rather than a core–shell or coated architecture.

## 4. CONCLUSIONS

For NiO precipitated at pH 8–11 and combined with a hydrothermally grown Mn-bearing phase, the main lesson of this work is that the precursor pH is not an effective processing variable over this window, and that the by-product content dominates the material. Three independent line-profile methods (Scherrer, Williamson–Hall, and size–strain plot) place the NiO crystallite size at 20–30 nm with a microstrain near $1\times10^{-3}$, and Nelson–Riley refinement gives a lattice parameter equal to that of bulk NiO within uncertainty; neither varies systematically with pH across the identically measured samples, although, with one batch per condition, an effect smaller than the unmeasured batch-to-batch scatter cannot be excluded. The residual NaCl content of the powders is large (32–41 wt% by a reference-intensity-ratio estimate) but varies non-monotonically, so the pH is not an effective lever on the by-product content either. FE-SEM at pH 8 and pH 9 showed sheet- and flake-like features after the hydrothermal step that are absent from the bare NiO; because the bare NiO already contains elongated features, and because the by-product phase is present in quantity, these features cannot be assigned to $MnO_2$ on morphological grounds.

The patterns of the hydrothermal product are dominated by a by-product phase whose reflections index on a primitive cubic cell of $a$ = 10.1175 Å, consistent with a langbeinite-type potassium–manganese sulfate. The two reflections attributable to tetragonal $MnO_2$ coincide with reflections of that cell, and the manganese detected by EDS can be hosted by the sulfate, so the presence of $MnO_2$ is not established by the present data. These by-product phases also preclude a reliable NiO crystallite-size determination in the hydrothermal products. The route therefore yields NiO together with Mn-bearing phases rather than a demonstrated NiO/$MnO_2$ composite, and by-product removal followed by phase redetermination—washing to a chloride-free rather than a pH-neutral end point, whole-pattern refinement, and a complementary technique such as Raman or infrared spectroscopy to identify the Mn-bearing phase directly—is a prerequisite for any claim of composite formation, as it is for surface-area measurement and for the electrochemical evaluation that motivates this route.

## AUTHOR CONTRIBUTIONS

**Bayu Prasetya:** Writing – original draft, Supervision. **Jihan F. Naila:** Investigation. **Resti Marlina:** Resources. **Wahyu S. Sipahutar:** Supervision. **Eka Nurfani:** Conceptualization, Supervision, Writing – original draft.

## CONFLICT OF INTEREST

The authors declare that they have no known competing financial interests or personal relationships that could have appeared to influence the work reported in this paper.

## DATA AVAILABILITY

Data will be made available on request.

## REFERENCES


[1] Yi C, Zou J, Yang H, Leng X. Recent advances in pseudocapacitor electrode materials: transition metal oxides and nitrides. *Trans. Nonferrous Met. Soc. China*. 2018;28(10):1980-2001. doi:10.1016/S1003-6326(18)64843-5.

[2] Chen R, Yu M, Sahu RP, Puri IK, Zhitomirsky I. The development of pseudocapacitor electrodes and devices with high active mass loading. *Adv. Energy Mater.* 2020;10(20):1903848. doi:10.1002/aenm.201903848.

[3] Zhao L, others. Honeycomb porous MnO2 nanofibers assembled from radially grown nanosheets for aqueous supercapacitors with high working voltage and energy density. *Nano Energy*. 2014;4:39-48. doi:10.1016/j.nanoen.2013.12.008.

[4] Yang X, Qiao Z, Liu F, Yang S, Zhang L, Cao B. In-depth study of electrochemical capacitor performance of MnO2 during phase transition from ramsdellite-MnO2 to birnessite-MnO2. *Electrochim. Acta*. 2018;280:77-85. doi:10.1016/j.electacta.2018.05.110.

[5] Li Y, Xu Z, Wang D, Zhao J, Zhang H. Snowflake-like core-shell alpha-MnO2@delta-MnO2 for high performance asymmetric supercapacitor. *Electrochim. Acta*. 2017;251:344-354. doi:10.1016/j.electacta.2017.08.146.

[6] Subramanian V, Zhu H, Wei B. Nanostructured MnO2: hydrothermal synthesis and electrochemical properties as a supercapacitor electrode material. *J. Power Sources*. 2006;159(1):361-364. doi:10.1016/j.jpowsour.2006.04.012.

[7] Ming B, Li J, Kang F, Pang G, Zhang Y, Chen L, Xu J, Wang X. Microwave-hydrothermal synthesis of birnessite-type MnO2 nanospheres as supercapacitor electrode materials. *J. Power Sources*. 2012;198:428-431. doi:10.1016/j.jpowsour.2011.10.003.

[8] Jiang H, Li C, Sun T, Ma J. A green and high energy density asymmetric supercapacitor based on ultrathin MnO2 nanostructures and functional mesoporous carbon nanotube electrodes. *Nanoscale*. 2012;4(3):807-812. doi:10.1039/c1nr11542a.

[9] Zhao Y, Meng Y, Jiang P. Carbon@MnO2 core-shell nanospheres for flexible high-performance supercapacitor electrode materials. *J. Power Sources*. 2014;259:219-226. doi:10.1016/j.jpowsour.2014.02.086.

[10] Nurfani E, Fau P, Khamidy NI, Marlina R. Effect of hydrothermal temperature on the structural and electrochemical properties of MnO2-based supercapacitors. *J. Mater. Sci. Mater. Electron.* 2024;35(32):2046. doi:10.1007/s10854-024-13820-w.

[11] Liu J, Jiang J, Bosman M, Fan HJ. Three-dimensional tubular arrays of MnO2–NiO nanoflakes with high areal pseudocapacitance. *J. Mater. Chem.* 2012;22(6):2419-2426. doi:10.1039/c1jm14804d.

[12] Yuan YF, others. Freestanding hierarchical NiO/MnO2 core/shell nanocomposite arrays for high-performance electrochemical energy storage. *Electrochim. Acta*. 2017;227:303-309. doi:10.1016/j.electacta.2017.01.002.

[13] Rahdar A, Aliahmad M, Azizi Y. NiO nanoparticles: synthesis and characterization. *J. Nanostruct.* 2015;5(2):145-151. doi:10.7508/jns.2015.02.009.

[14] Salavati-Niasari M, Entesari M. Controlled synthesis of spherical alpha-Ni(OH)2 hierarchical nanostructures via a simple hydrothermal process and their conversion to NiO. *Polyhedron*. 2012;33(1):302-309. doi:10.1016/j.poly.2011.11.054.

[15] Chai H, Chen X, Jia D, Bao S, Zhou W. Flower-like NiO structures: controlled hydrothermal synthesis and electrochemical characteristic. *Mater. Res. Bull.* 2012;47(12):3947-3951. doi:10.1016/j.materresbull.2012.08.033.

[16] Cheng G, Yan Y, Chen R. From Ni-based nanoprecursors to NiO nanostructures: morphology-controlled synthesis and structure-dependent electrochemical behavior. *New J. Chem.* 2015;39(1):676-682. doi:10.1039/c4nj01398k.

[17] Soomro RA, Ibupoto ZH, Sirajuddin, Abro MI, Willander M. Controlled synthesis and electrochemical application of skein-shaped NiO nanostructures. *J. Solid State Electrochem.* 2015;19(3):913-922. doi:10.1007/s10008-014-2700-z.

[18] Patel KN, Deshpande MP, Gujarati VP, Pandya S, Sathe V, Chaki SH. Structural and optical analysis of Fe doped NiO nanoparticles synthesized by chemical precipitation route. *Mater. Res. Bull.* 2018;106:187-196. doi:10.1016/j.materresbull.2018.06.003.

[19] Sathishkumar K, Shanmugam N, Kannadasan N, Cholan S, Viruthagiri G. Synthesis and characterization of Cu2+ doped NiO electrode for supercapacitor application. *J. Sol-Gel Sci. Tech-*


© 2026 The Authors | CC-BY 4.0

*nol*. 2015;74(3):621-630. doi:10.1007/s10971-015-3641-4.

[20] Liu T, Jiang C, Cheng B, You W, Yu J. Hierarchical flower-like C/NiO composite hollow microspheres and its excellent supercapacitor performance. *J. Power Sources*. 2017;359:371-378. doi:10.1016/j.jpowsour.2017.05.100.

[21] Kitchamsetti N, Chikate PR, Patil RA, Ma YR, Shirage PM, Devan RS. Perforated mesoporous NiO nanostructures for an enhanced pseudocapacitive performance with ultra-high rate capability and high energy density. *CrystEngComm*. 2019;21(46):7130-7140. doi:10.1039/c9ce01475f.

[22] Keshari AS, Dubey P. Rapid microwave-assisted vs. hydrothermal synthesis of hierarchical sheet-like NiO/NiMoO4 hybrid nanostructures for high performance extrinsic pseudocapacitor application. *J. Energy Storage*. 2021;40:102629. doi:10.1016/j.est.2021.102629.

[23] Padmanathan N, Selladurai S. Electrochemical capacitance of porous NiO-CeO2 binary oxide synthesized via sol-gel technique for supercapacitor. *Ionics*. 2014;20(3):409-420. doi:10.1007/s11581-013-0989-8.

[24] Nurfani E, Grace G, Darmawan MY, Marlina R, Jatmika J, Rinovian A, Rianjanu A. Structural, optical, and electrical properties of Cu-doped NiO films synthesized by spray pyrolysis for potential gas sensing applications. *Next Mater.* 2026;13:102670. doi:10.1016/j.nxmate.2026.102670.

[25] Zhang B, others. NiO/MnO2 core/shell nanocomposites for high-performance pseudocapacitors. *Mater. Lett.* 2014;114:40-43. doi:10.1016/j.matlet.2013.09.107.

[26] Chen J, Huang Y, Li C, Chen X, Zhang X. Synthesis of NiO@MnO2 core/shell nanocomposites for supercapacitor application. *Appl. Surf. Sci.* 2016;360:534-539. doi:10.1016/j.apsusc.2015.10.187.

[27] Yi TF, Mei J, Guan B, Cui P, Luo S, Xie Y, Liu Y. Construction of spherical NiO@MnO2 with core-shell structure obtained by depositing MnO2 nanoparticles on NiO nanosheets for high-performance supercapacitor. *Ceram. Int.* 2020;46(1):421-429. doi:10.1016/j.ceramint.2019.08.278.

[28] Padmanathan N, Selladurai S. Solvothermal synthesis of mesoporous NiCo2O4 spinel oxide nanostructure for high-performance electrochemical capacitor electrode. *Ionics*. 2013;19(11):1535-1544. doi:10.1007/s11581-013-0907-0.

[29] Han L, Tang P, Zhang L. Hierarchical Co3O4@PPy@MnO2 core-shell-shell nanowire arrays for enhanced electrochemical energy storage. *Nano Energy*. 2014;7:42-51. doi:10.1016/j.nanoen.2014.04.014.

[30] Feng M, Zhang G, Du Q, Su L, Ma Z, Qin X, Shao G. Co3O4@MnO2 core shell arrays on nickel foam with excellent electrochemical performance for aqueous asymmetric supercapacitor. *Ionics*. 2017;23(7):1637-1643. doi:10.1007/s11581-017-2013-1.

[31] Wu X, Meng L, Wang Q, Zhang W, Wang Y. High flexibility and large energy density asymmetric fibered-supercapacitor based on unique NiCo2O4@MnO2 core-shell nanobrush arrays electrode. *Electrochim. Acta*. 2019;295:532-539. doi:10.1016/j.electacta.2018.10.196.

[32] Tao B, He J, Miao F, Zhang Y. MnO2/NiCo2O4 loaded on nickel foam as a high-performance electrode for advanced asymmetric supercapacitor. *Vacuum*. 2022;195:110668. doi:10.1016/j.vacuum.2021.110668.

[33] Vamsikrishna K, Usha P, Venkatesh D, Ramesh T. Structural, morphological, optical, and magnetic properties of NiO-added NiCo2O4 electrode materials synthesized by sol-gel, co-precipitation and ultrasonication methods and their electrochemical supercapacitor response. *Ceram. Int.* 2024;50(17):30869-30878. doi:10.1016/j.ceramint.2024.05.392.

[34] Dubal DP, Holze R, Gomez-Romero P. Three-dimensional arrays of 1D MnO2 nanocrystals for all-solid-state asymmetric supercapacitors. *ChemPlusChem*. 2015;80(6):944-951. doi:10.1002/cplu.201500054.

[35] Gan YX, Jayatissa AH, Yu Z, Chen X, Li M. Hydrothermal synthesis of nanomaterials. *J. Nanomater.* 2020;2020:8917013. doi:10.1155/2020/8917013.

[36] Aini Q, Putri CIS, Nurfitria R, Hanifah IR. Influence of Nb dopant concentration on the structural properties and photocatalytic performances of hydrothermally synthesized ZnO for multi-pollutant degradation. *Greensusmater*. 2026;3(1). doi:10.62755/gsm.2026.01.

[37] Anastasya Y, Muhtar SA, Munandar A, Saraswati AR, Taher T. Hydrothermal synthesis of Nb2O5-natural zeolite composite for enhanced adsorptive removal of anionic and cationic dye. *Greensusmater*. 2024;1(2):63-67. doi:10.62755/greensusmater.2024.1.2.63-67.

[38] Cheng B, Samulski ET. Hydrothermal synthesis of one-dimensional ZnO nanostructures with different aspect ratios. *Chem. Commun.* 2004:986-987. doi:10.1039/b316435g.

[39] Pellegrino F, Sordello F, Mino L, Prozzi M, Mansfeld U, Hodoroaba VD, Minero C. Polyethylene glycol as shape and size controller for the hydrothermal synthesis of SrTiO3 cubes and polyhedra. *Nanomaterials*. 2020;10(9):1892. doi:10.3390/nano10091892.

[40] Sun P, Lv Z, Sun C. Study on the synthesis of nano zinc oxide particles under supercritical hydrothermal conditions. *Nanomaterials*. 2024;14(10):844. doi:10.3390/nano14100844.

[41] Oktapia D, Nurfani E, Wahjoedi BA, Nulhakim L, Kadja GTM. Seedless hydrothermal growth of hexagonal prism ZnO for photocatalytic degradation of methylene blue: the effect of pH and post-annealing treatment. *Semicond. Sci. Technol.* 2023;38(10):105005. doi:10.1088/1361-6641/acf397.

[42] Khan MGI, others. Hydrothermal synthesis of CeO2/ZnO heterojunctions for effective photocatalytic degradation of organic pollutants. *Mater. Sci. Eng. B*. 2025;322:118630. doi:10.1016/j.mseb.2025.118630.

[43] Phasa A, Aini Q, Siregar MY, Sabilla S, Triyadi D, Aflaha R, Khan MGI, Nurfani E. Photocatalytic degradations of organic pollutants in wastewater using hydrothermally grown ZnO nanoparticles. *Greensusmater*. 2024;1(2):39-43. doi:10.62755/greensusmater.2024.1.2.39-43.

[44] Fitri A, Lumbanraja FR, Hanifah IR, Prasetya B, Aflaha R, Putra SEM. Congo red dye adsorption using ZnAl layered double hydroxide fabricated using hydrothermal methods. *Greensusmater*. 2024;1(2):44-50. doi:10.62755/greensusmater.2024.1.2.44-50.

[45] Al Mubarok MR, Nurfitria R, Aflaha R, Nurfani E, Rianjanu A. Niobium oxide electrode performance boosted by molybdenum doping and calcination for supercapacitor applications. *Greensusmater*. 2025;2(2):62-69. doi:10.62755/greensusmater.2025.2.2.62-69.

[46] Rianjanu A, Nuraeni R, Aflaha R, Khamidy NI, Triyana K, Taher T. Effect of calcination temperature on the performance of hydrothermally grown cerium dioxide (CeO2) nanorods for the removal of Congo red dyes. *Greensusmater*. 2024;1(1):9-14. doi:10.62755/greensusmater.2024.1.1.9-14.

[47] Widakdo J. Thermal annealing tailors crystallinity and magnetism in silica coated Ni-Zn ferrite (SiO2@NiZnFe2O4) nanoparticles. *Greensusmater*. 2025;2(2):30-35. doi:10.62755/greensusmater.2025.2.2.30-35.

[48] Sharma RK, Ghose R. Synthesis of Co3O4-ZnO mixed metal oxide nanoparticles by homogeneous precipitation method. *J. Alloys Compd.* 2016;686:64-73. doi:10.1016/j.jallcom.2016.05.298.

[49] Petcharoen K, Sirivat A. Synthesis and characterization of magnetite nanoparticles via the chemical co-precipitation method. *Mater. Sci. Eng. B*. 2012;177(5):421-427. doi:10.1016/j.mseb.2012.01.003.

[50] Mascolo MC, Pei Y, Ring TA. Room temperature co-precipitation synthesis of magnetite nanoparticles in a large pH window with different bases. *Materials*. 2013;6(12):5549-5567. doi:10.3390/ma6125549.

[51] Thanh NTK, Maclean N, Mahiddine S. Mechanisms of nucleation and growth of nanoparticles in solution. *Chem. Rev.* 2014;114(15):7610-7630. doi:10.1021/cr400544s.

[52] Arshadi S, Moghaddam J, Eskandarian M. LaMer diagram approach to study the nucleation and growth of Cu2O

© 2026 The Authors | CC-BY 4.0 

nanoparticles using supersaturation theory. *Korean J. Chem. Eng.* 2014;31(11):2020-2026. doi:10.1007/s11814-014-0130-3.

[53] Sharifi Dehsari H, Ribeiro AH, Ersöz B, Tremel W, Jakob G, Asadi K. Effect of precursor concentration on size evolution of iron oxide nanoparticles. *CrystEngComm*. 2017;19(44):6694-6702. doi:10.1039/c7ce01406f.

[54] Isley SL, Penn RL. Titanium dioxide nanoparticles: effect of sol-gel pH on phase composition, particle size, and particle growth mechanism. *J. Phys. Chem. C*. 2008;112(12):4469-4474. doi:10.1021/jp710844d.

[55] Rani S, Varma GD. Superparamagnetism and metamagnetic transition in Fe3O4 nanoparticles synthesized via co-precipitation method at different pH. *Physica B*. 2015;472:66-77. doi:10.1016/j.physb.2015.05.016.

[56] Samaele N, Amornpitoksuk P, Suwanboon S. Effect of pH on the morphology and optical properties of modified ZnO particles by SDS via a precipitation method. *Powder Technol.* 2010;203(2):243-247. doi:10.1016/j.powtec.2010.05.014.

[57] Manchwari S, Khatter J, Chauhan RP. Modifications in structural, morphological and optical properties of TiO2 nanoparticles: effect of pH. *Chem. Pap.* 2022;76(12):7545-7551. doi:10.1007/s11696-022-02437-0.

[58] Nurfani E, Ali MP, Rianjanu A, Nulhakim L, Anrokhi MS, Kadja GTM. Effect of solution molarity on the optical and photocatalytic properties of sprayed ZnO film. *Mater. Chem. Phys.* 2023;309:128412. doi:10.1016/j.matchemphys.2023.128412.

[59] Ali MP, Rianjanu A, Pertiwi N, Kurniawan R, Marlina R, Nurfani E. Optical and photocatalytic properties of ZnO:Mg film grown by spray pyrolysis. *J. Iran. Chem. Soc.* 2024;21(10):2733-2741. doi:10.1007/s13738-024-03105-8.

[60] Saputra IS, Nurfani E, others. Effect of secondary metabolites from several leaf extracts on the green synthesized-ZnO nanoparticles. *Vacuum*. 2024;227:113434. doi:10.1016/j.vacuum.2024.113434.

[61] Pescke IK, de Oliveira Rozino L, Zenato K, Cardozo T, Flores WH, Vargas VMF. Lowering the pH leads to the disaggregation of NiO and ZnO nanoparticles and modifies the mutagenic response. *J. Appl. Toxicol.* 2024;44(3):445-454. doi:10.1002/jat.4553.

[62] Yogamalar R, Srinivasan R, Vinu A, Ariga K, Bose AC. X-ray peak broadening analysis in ZnO nanoparticles. *Solid State Commun.* 2009;149(43–44):1919-1923. doi:10.1016/j.ssc.2009.07.043.

[63] Khorsand Zak A, Abd. Majid WH, Abrishami ME, Yousefi R. X-ray analysis of ZnO nanoparticles by Williamson-Hall and size-strain plot methods. *Solid State Sci.* 2011;13(1):251-256. doi:10.1016/j.solidstatesciences.2010.11.024.

[64] Rajesh Kumar B, Hymavathi B. X-ray peak profile analysis of solid-state sintered alumina doped zinc oxide ceramics by Williamson-Hall and size-strain plot methods. *J. Asian Ceram. Soc.* 2017;5(2):94-103. doi:10.1016/j.jascer.2017.02.001.

[65] Irfan H, Mohamed Racik K, Anand S. X-ray peak profile analysis of CoAl2O4 nanoparticles by Williamson-Hall and size-strain plot methods. *Mod. Electron. Mater.* 2018;4(1):31-40. doi:10.3897/j.moem.4.1.33272.

[66] Srinivasan R, Yogamalar NR, Justin Joseyphus R, Bose AC. Estimation of lattice strain, stress, energy density and crystallite size of the spherical yttrium oxide nanoparticles. *Funct. Mater. Lett.* 2009;2(3):131-134. doi:10.1142/S1793604709000673.

[67] Hossain MS, Ahmed S. Easy and green synthesis of TiO2 (anatase and rutile): estimation of crystallite size using Scherrer equation, Williamson-Hall plot, Monshi-Scherrer model, size-strain plot, Halder-Wagner model. *Results Mater.* 2023;20:100492. doi:10.1016/j.rinma.2023.100492.

[68] Kinasih DAS, Nurhasanah I. Estimasi ukuran kristal dan parameter elastisitas nanokristal ZnO:Ce menggunakan metode size-strain plot. *Berkala Fisika*. 2020;23(2):56-62.

[69] John KI, Adenle AA, Adeleye AT, Onyia IP, Amune-Matthews C, Omorogie MO. Unravelling the effect of crystal dislocation density and microstrain of titanium dioxide nanoparticles on tetracycline removal performance. *Chem. Phys. Lett.* 2021;776:138725. doi:10.1016/j.cplett.2021.138725.

[70] Azizah N, Muhammady S, Purbayanto MAK, Nurfani E, Winata T, Sustini E, Widita R, Darma Y. Influence of Al doping on the crystal structure, optical properties, and photodetecting performance of ZnO film. *Prog. Nat. Sci. Mater. Int.* 2020;30(1):28-34. doi:10.1016/j.pnsc.2020.01.006.

[71] Nurfani E, Lailani A, Kesuma WAP, Anrokhi MS, Kadja GTM, Rozana M. UV sensitivity enhancement in Fe-doped ZnO films grown by ultrafast spray pyrolysis. *Opt. Mater.* 2021;112:110768. doi:10.1016/j.optmat.2020.110768.

[72] Nurfani E, Firdaus AR, Triyadi D, Rianjanu A. Role of Ni dopant on the improvement of ZnO-based reusable photocatalytic materials. *Greensusmater*. 2024;1(2):51-56. doi:10.62755/greensusmater.2024.1.2.51-56.

[73] Kurnia NR, Amanda T, Nurfitria R, Aflaha R, Widakdo J, Rianjanu A. Development and materials characterization of hydrothermally grown niobium-doped BiVO4 for ciprofloxacin and methylene blue degradation. *Greensusmater*. 2025;2(2):55-61. doi:10.62755/greensusmater.2025.2.2.55-61.

[74] Nelson JB, Riley DP. An experimental investigation of extrapolation methods in the derivation of accurate unit-cell dimensions of crystals. *Proc. Phys. Soc.* 1945;57(3):160-177. doi:10.1088/0959-5309/57/3/302.

[75] Langford JI, Wilson AJC. Scherrer after sixty years: a survey and some new results in the determination of crystallite size. *J. Appl. Crystallogr.* 1978;11(2):102-113. doi:10.1107/S0021889878012844.

[76] Williamson GK, Hall WH. X-ray line broadening from filed aluminium and wolfram. *Acta Metall.* 1953;1(1):22-31. doi:10.1016/0001-6160(53)90006-6.

[77] Chung FH. Quantitative interpretation of X-ray diffraction patterns of mixtures. I. Matrix-flushing method for quantitative multicomponent analysis. *J. Appl. Crystallogr.* 1974;7(6):519-525. doi:10.1107/S0021889874010375.

[78] Kumar M, Kumar A, Abhyankar AC. Influence of texture coefficient on surface morphology and sensing properties of W-doped nanocrystalline tin oxide thin films. *ACS Appl. Mater. Interfaces*. 2015;7(6):3571-3580. doi:10.1021/am507397z.

[79] McMurdie HF, Morris MC, deGroot J, Swanson HE. Crystallography of some double sulfates and chromates. *J. Res. Natl. Bur. Stand. Sect. A Phys. Chem.* 1971;75A(5):435-439. doi:10.6028/jres.075A.034.

[80] CRC Handbook of Chemistry and Physics. 2016. doi:10.1201/9781315380476.

[81] Reichle RA, McCurdy KG, Hepler LG. Zinc hydroxide: solubility product and hydroxy-complex stability constants from 12.5–75 °C. *Can. J. Chem.* 1975;53(24):3841-3845. doi:10.1139/v75-556.

[82] Wang X, Li Y. Selected-control hydrothermal synthesis of alpha- and beta-MnO2 single crystal nanowires. *J. Am. Chem. Soc.* 2002;124(12):2880-2881. doi:10.1021/ja0177105.

© 2026 The Authors | CC-BY 4.0 